Measurement of the cosmic ray energy spectrum using hybrid events of the Pierre Auger Observatory

C. Bleve [1,2], G. Cataldi[2], G. Cocciolo[2,3], M. R. Coluccia[1,2], P. Creti[2], S. D'Amico[2,3] I. De Mitri[1,2], G. Marsella[1,2], D. Martello[1,2], L.Perrone[1,2], V. Scherini[1,2] and the Pierre Auger Collaboration

[1] Dipartimento di Matematica e Fisica "Ennio De Giorgi", Università del Salento, Italy
[2] Istituto Nazionale di Fisica Nucleare sez. di Lecce, Italy
[3] Dipartimento di Ingegneria dell'Innovazione Università del Salento, Italy

1. Abstract

The flux of cosmic rays above 3×10^{17} eV has been measured with unprecedented precision at the Pierre Auger Observatory based on data in the period between 1 January 2004 and 31 December 2012. The unique combination of different nested detector arrangements has been used to record cosmic ray data spanning over an energy range of almost three decades. The hybrid nature of the instrument has been exploited to determine the energy in a data-driven mode with minimal Monte Carlo input. The spectral features are presented in detail and the impact of systematic uncertainties on these features is addressed [1].

2. Introduction

The measurement of the energy spectrum of ultra-high energy cosmic rays addresses fundamental questions about the origin and propagation of these particles, as well as about physical properties of accelerators and particle cross-sections at the highest energies. The most distinct features of the flux above 10^{18} eV are a flattening of the spectrum at 4×10^{18} eV (the *ankle*) and a strong flux suppression above 5×10^{19} eV which is often attributed to the GZK cut-off but might also be due to the maximum source energy [2–4]. The exact physical explanation of the observed spectral features remains uncertain. Also, the transition from galactic to extra-galactic cosmic rays may occur between 10^{17} eV and the ankle. A precise measurement of the flux at energies above 10^{17} eV is important for discriminating between different theoretical models [5–8].

The Pierre Auger Observatory is a hybrid detector employing two complementary detection techniques for the ground-based measurement of air showers induced by UHECRs, a *surface detector array* (SD) and a *fluorescence detector* (FD).

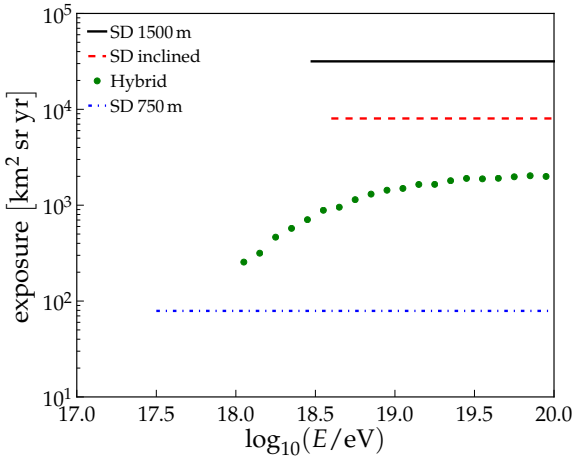

Figure 1. The integrated exposure of the different detectors at the Pierre Auger Observatory as a function of energy. The SD exposure in the three cases is flat above the energy corresponding to full trigger efficiency for the surface arrays. Values and zenith angle ranges are given in Table 1.

The SD is an array of 10 m^2 water Cherenkov detectors. 1600 detectors are arranged in a hexagonal grid with spacing of 1500 m, covering a total area of 3000 km^2. This array is fully efficient at energies above 3×10^{18} eV [9]. 49 additional detectors with 750 m spacing have been nested within the 1500 m array to cover an area of 25 km^2 with full efficiency above 3×10^{17} eV [10]. The SD array is sensitive to electromagnetic and muonic secondary particles of air showers and has a duty cycle of almost 100% [11,12]. The SD is overlooked by 27 optical telescopes grouped in 5 buildings on the periphery of the array. The FD is sensitive to the fluorescence light emitted by nitrogen molecules that are excited by secondary particles of the shower and to the Cherenkov light induced by these particles. This allows for the observa-

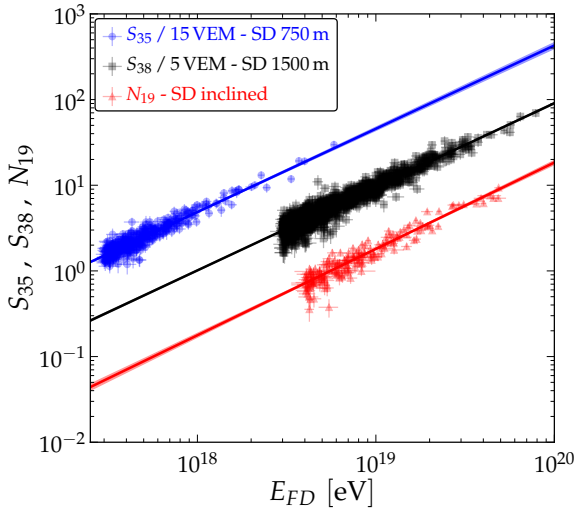

Figure 2. The correlation between the different energy estimators S_{38}, S_{35} and N_{19} (see text) and the energy determined by FD.

tion of the longitudinal development of air showers during clear and moonless nights, resulting in a duty cycle of about 13% [13,14].

We present the measurement of the flux of cosmic rays above $3{\times}10^{17}$ eV, obtained by combining data from these detectors. The dataset extends from 1 January 2004 to 31 December 2012, thus updating earlier measurements.

3. Flux measurements with the SD array

The reconstruction of arrival direction and core position of air showers measured with the SD array is performed using the trigger times and signals recorded by individual detector stations. Signals are calibrated in units of VEM, corresponding to the signal produced by a Vertical Equivalent Muon [12,15]. Different attenuation characteristics of the electromagnetic and muonic shower components lead to different reconstruction methods for different zenith angle ranges. In the following we distinguish between *vertical events* ($\theta < 60°$) and *inclined events* ($62° \leq \theta < 80°$).

The energy reconstruction of vertical events is based on the estimation of the lateral distribution of secondary particles of an air shower reaching ground at an optimal distance to the shower core. The optimal distances are those at which, for a wide range of reasonable lateral distribution functions, the spread in this signal size predicted at that distance is a minimum. For the 1500 m and 750 m arrays the optimal distances, determined empirically, are 1000 m and 450 m respectively. See [16,17] for details. The signals $S(1000)$ and $S(450)$ are corrected for their zenith angle dependence due to air shower attenuation in the atmosphere with a Constant Intensity Cut (CIC) method [18]. The equivalent signal at median zenith angle of 38° (35°) is used to infer the energy for the 1500 m (750 m) array [10,19,20]. Note that for the 750 m array, only events with zenith angle below 55° are accepted. Variations of the shape of the attenuation function due to the change of the average maximum depth of shower development with energy are below 5% for the considered zenith angles.

Inclined air-showers are characterized by the dominance of secondary muons at ground, as the electromagnetic component is largely absorbed in the large atmospheric depth traversed by the shower [21]. The reconstruction is based on the estimation of the relative muon content N_{19} with respect to a simulated proton shower with energy 10^{19} eV [22]. N_{19} is used to infer the primary energy for inclined events. Due to the limited exposure of the 750 m array only inclined events from the 1500 m array are included in the present analysis.

Events, both vertical and inclined, are selected if the detector with the highest signal is enclosed in a hexagon of six active stations. The exposure is obtained by integrating the effective area (i.e. the sum of the areas of all active hexagons) over observation time [9]. Exposures of the SD array for the different datasets are shown in Fig. 1. Values up to 31 Dec 2012 are given in Table 1 together with their uncertainties and the relevant zenith angle ranges. In case of vertical events measured with the 1500 m array the integrated exposure amounts to an increase of 50% with respect to the previous publication [2,23]. The number of events above $3{\times}10^{18}$ eV does not fully reflect this increase due to changes in the energy scale and calibration [24].

Events that have independently triggered the SD array and FD telescopes (called golden hybrid events) are used for the energy calibration of SD data. Only a sub-sample of events that pass strict quality and field of view selections are used [10,19]. The relations between the different energy estimators $\hat{E}$, i.e. S_{38}, S_{35}, N_{19}, and the energies reconstructed from the FD measurements $E_{\rm FD}$ are well described by power-laws $E_{\rm FD} = A \cdot \hat{E}^B$. The calibration parameters are given in Table 1 together with the number of golden hybrid events. The correlation between the different energy estimators and $E_{\rm FD}$ is shown in Fig. 2 superimposed with the calibration functions resulting from maximum-likelihood fits. For the vertical events of the 1500 m array, the SD

	Auger SD			Auger hybrid
	1500 m vertical	**1500 m inclined**	**750 m vertical**	
Data taking period	01/2004 - 12/2012	01/2004 - 12/2012	08/2008 - 12/2012	11/2005 - 12/2012
Exposure $[\mathrm{km^2\ sr\ yr}]$	31645 ± 950	8027 ± 240	79 ± 4	see Fig. 1
Zenith angles [°]	$0 - 60$	$62 - 80$	$0 - 55$	$0 - 60$
Threshold energy E_{eff} [eV]	3×10^{18}	4×10^{18}	3×10^{17}	10^{18}
No. of events ($E > E_{\mathrm{eff}}$)	82318	11074	29585	11155
No. of events (golden hybrids)	1475	175	414	-
Energy calibration (A) [EeV]	0.190 ± 0.005	5.61 ± 0.1	$(1.21 \pm 0.07) \cdot 10^{-2}$	-
Energy calibration (B)	1.025 ± 0.007	0.985 ± 0.02	1.03 ± 0.02	-

Table 1
Summary of the experimental parameters describing data of the different measurements at the Pierre Auger Observatory. Numbers of events are given above the energies corresponding to full trigger efficiency.

energy resolution due to limited sampling statistics decreases from 15% below 6×10^{18} eV to less than 12% above 10^{19} eV [25]. Physical fluctuations in shower development are the major contribution at highest energies with $\approx 12\%$. In case of inclined events, physical fluctuations are larger, $\approx 16\%$ [22].

To check the energy reconstruction and intrinsic resolutions, the reconstruction was also performed using simulated events. For vertical events of the 1500 m array, the distribution of the ratio of the inferred SD energy E_{SD} and the reconstructed FD energy E_{FD} is compared to Monte-Carlo simulations in Fig. 3. Due to the lack of muons in simulations compared to data (e.g. [26]), the SD energy scale of simulations was rescaled by 24% (averaging primaries and energies) to match that of data. Based on this rescaling, the observed distributions are well reproduced by Monte-Carlo simulations.

Due to the steepness of the energy spectrum and the finite resolution of the SD measurements, the measured spectra represent a smearing of the true spectrum due to bin-to-bin migrations. Corrections have been applied to obtain the true energy spectrum [2]. These are below 15% in the energy range of interest.

The energy spectra obtained from the three SD datasets are shown in Fig. 4. Due to the calibration with events observed by the FD, the SD energies share the uncertainty of the FD energy scale of 14%, which will be further explained in the next section.

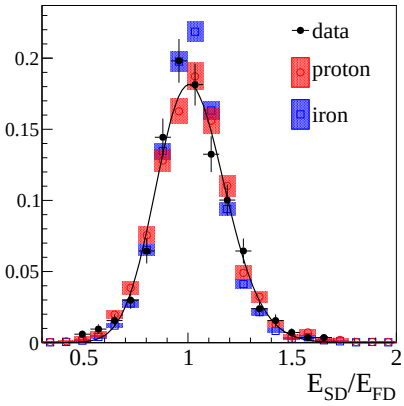

Figure 3. Distribution of the ratio between the reconstructed SD and FD energy, E_{SD} and E_{FD}. Ratios are obtained from data and QGSJet-II.03 simulations [27] (see text).

4. Flux measurements with the hybrid detector

The hybrid approach is based on the detection of showers observed by the FD in coincidence with at least one station of the SD array. Although a signal in a single station does not allow an independent trigger and reconstruction in SD, it is a sufficient condition for a very accurate determination of the shower geometry using the hybrid reconstruction.

To ensure good energy reconstruction, only events that satisfy strict quality criteria are accepted [14]. In particular, to avoid a possible bias in event selection due to the differences between shower profiles initiated by primaries of different mass, a shower is retained only if its geometry would allow a reliable measurement of any shower profile that occurs in the full data set. A detailed simulation of the detector response has shown that for zenith angles less than 60°, every FD event above 10^{18} eV passing all the selection criteria is triggered by at least one SD station, independent of the mass or direction of the incoming primary particle [14].

The measurement of the flux of cosmic rays us-

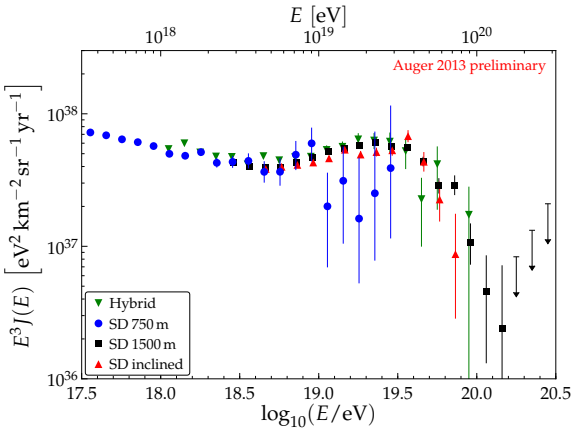

Figure 4. Energy spectra, corrected for energy resolution, derived from SD and from hybrid data.

ing hybrid events relies on the precise determination of the detector exposure that is influenced by several factors. The response of the hybrid detector strongly depends on energy and distance from the relevant fluorescence telescope, as well as atmospheric and data taking conditions. To properly take into account all of these configurations and their time variability, the exposure has been calculated using a sample of simulated events that reproduce the exact conditions of the experiment [14]. The total systematic uncertainty on the calculation of the exposure ranges from 14% at 10^{18} eV to below 6% above 10^{19} eV [14]. The current hybrid exposure as a function of energy is shown in Fig. 1 compared with the exposures of the surface detectors.

The energy spectrum reconstructed from hybrid events will be presented at the conference and in the updated version of this paper. Data taken in the time period given in Table 1 are included. The main systematic uncertainty is due to the energy assignment which relies on the knowledge of the fluorescence yield (3.6%), atmospheric conditions (3%-6%), absolute detector calibration (9%) and shower reconstruction (6%) [24]. The invisible energy is calculated with a new, simulation-driven but model-independent method with an uncertainty of 1.5%-3% [28].

5. Combined energy spectrum

The hybrid spectrum extends the SD 1500 m spectrum below the energy of full trigger efficiency of 3×10^{18} eV and overlaps with the spectrum of the 750 m array above 10^{18} eV. The latter is fitted up to 3×10^{18} eV and extends the measurement of the energy spectrum below 10^{18} eV. The spectrum of inclined events contributes above its full efficiency threshold of 4×10^{18} eV and provides an independent measurement in this energy range. We combine these measurements into a single energy spectrum.

The SD measurements are affected by uncertainties due to the energy calibrations (see Table 1). These uncertainties are taken into account by minimizing the energy calibration likelihoods together with the smearing corrections due to bin-to-bin migrations. In this combined maximum-likelihood fit, the normalizations of the different spectra are allowed to vary within the exposure uncertainties as stated in Table 1.

The combined energy spectrum is shown in Fig. 5 together with the number of observed events within each bin. To characterize the spectral features we describe the data with a power law below the ankle $J(E) \propto E^{-\gamma_1}$ and a power law with smooth suppression above:

$$J(E; E > E_a) \propto E^{-\gamma_2} \left[1 + \exp\left(\frac{\log_{10} E - \log_{10} E_{1/2}}{\log_{10} W_c}\right)\right]^{-1}. \quad (1)$$

γ_1, γ_2 are the spectral indices below/above the ankle at E_a. $E_{1/2}$ is the energy at which the flux has dropped to half of its peak value before the suppression, the steepness of which is described with $\log_{10} W_c$.

The resulting spectral parameters are given in Table 2. To match the energy spectra, the SD 750 m spectrum has to be scaled up by 2%, the inclined spectrum up by 5% and the hybrid spectrum down by 6%. Compared to the previous publication, the precision in determining the spectral index below the ankle has increased significantly, mainly due to the addition of the 750 m array. We report a slightly flatter spectrum below the ankle (now: 3.23 ± 0.01 (stat) ± 0.07 (sys), previous publication: 3.27 ± 0.02) and an increase of E_a (now: 18.72 ± 0.01 (stat) ± 0.02 (sys), previous publication: 18.61 ± 0.01) [23]. The large systematic uncertainties in γ_1 are dominated by the uncertainty of the resolution model used for correcting the measured flux. At the same time, the uncertainty in the energy scale of 14% is propagated into the final result.

The combined energy spectrum is compared to fluxes from three astrophysical scenarios in Fig. 6. Shown are models assuming pure proton or iron composition and a maximum injection energy of 10^{20} eV. The fluxes result from different assumptions of the spectral index β of the source injection spectrum and the source evolution parameter m. The model lines have been calculated using CRPropa [31] and validated with SimProp [32].

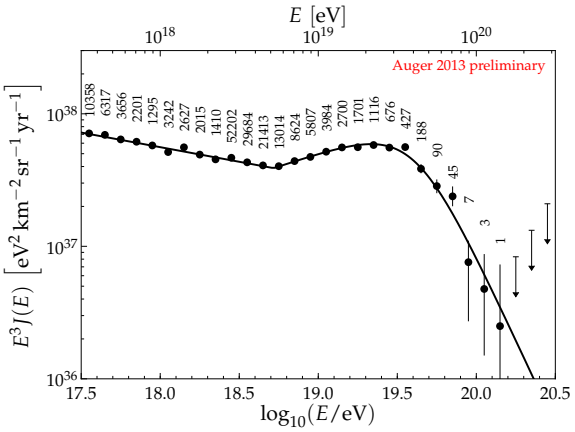

Figure 5. The combined energy spectrum of UHECRs as measured at the Pierre Auger Observatory. The numbers give the total number of events inside each bin. The last three arrows represent upper limits at 84% C.L.

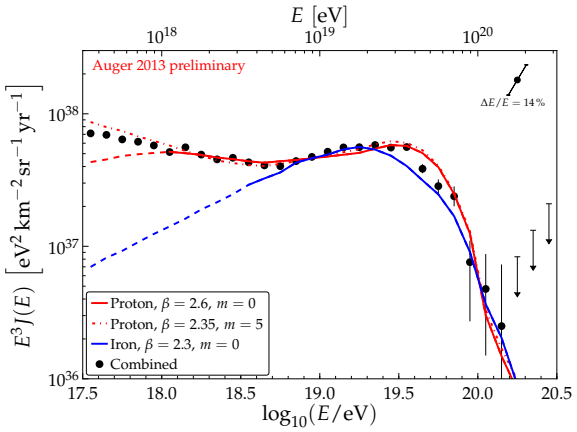

Figure 6. The combined energy spectrum compared to energy spectra from different astrophysical scenarios (see text).

Parameter	**Result** $(\pm\sigma_{\rm stat} \pm \sigma_{\rm sys})$
$\log_{10}(E_{\rm a}/{\rm eV})$	$18.72 \pm 0.01 \pm 0.02$
γ_1	$3.23 \pm 0.01 \pm 0.07$
γ_2	$2.63 \pm 0.02 \pm 0.04$
$\log_{10}(E_{1/2}/{\rm eV})$	$19.63 \pm 0.01 \pm 0.01$
$\log_{10} W_c$	$0.15 \pm 0.01 \pm 0.02$

Table 2
Parameters, with statistical and systematic uncertainties, of the model describing the combined energy spectrum measured at the Pierre Auger Observatory.

6. Summary

The flux of cosmic rays above 3×10^{17} eV has been measured at the Pierre Auger Observatory combining data from surface and fluorescence detectors. The spectral features are determined with unprecedented statistical precision. The fitted parameters are compatible with previous results given the change in the energy scale. There is an overall uncertainty of the revised energy scale of 14% [24]. Current results from $X_{\rm max}$ measurements and an interpretation of the measurements concerning mass composition are presented in [29,30]. The spectrum as measured with the SD 750 m array is presented in more detail at this conference in [10].

REFERENCES

1. A. Schulz, for the Pierre Auger Collaboration, Proc. 33rd ICRC, Rio de Janeiro, Brazil, (2013); arXiv:1307.5059.
2. The Pierre Auger Collaboration, Phys.Lett. **B685** (2010) 239, arXiv:1002.1975.
3. R. U. Abbasi et al., High Resolution Flys Eye Collaboration, Phys. Rev. Lett. **100** (2008) 101101.
4. T. Abu-Zayyad et al., Astrophys. J. **768** (2013) L1, arXiv:1205.5067.
5. V. Berezinsky, A. Z. Gazizov, and S. I. Grigorieva, Phys. Lett. **B612** (2005) 147.
6. A. M. Hillas, J. Phys. **G31** (2005) R95.
7. T. Wibig and A. W. Wolfendale, J. Phys., **G31** (2005) 255.
8. D. Allard et al., JCAP **0810** (2008) 033.
9. The Pierre Auger Collaboration, Nucl. Instr. and Meth. **A613** (2010) 29.
10. D. Ravignani, for the Pierre Auger Collaboration, paper 0693, Proc. 33rd ICRC, Rio de Janeiro, Brazil, (2013); arXiv:1307.5059.
11. The Pierre Auger Collaboration, Nucl. Instr. Meth. **A523** (2004) 50.
12. I. Allekotte et al., Nucl. Instr. Meth. **A586** (2008) 409.
13. The Pierre Auger Collaboration, Nucl. Instr. Meth. **A620** (2010) 227.
14. The Pierre Auger Collaboration, Astropart. Phys. **34** (2011) 368.
15. X. Bertou et al., Nucl. Instr. Meth. **A568** (2006) 839.
16. A.M. Hillas, Acta Physica Academiae Scientiarum Hungaricae **26** (1970) 355.
17. D. Newton, J. Knapp, A.A. Watson, Astropart. Phys. **26**, 414 (2007).
18. J. Hersil et al., Phys. Rev. Lett. **6**, 22 (1961).
19. R. Pesce, for the Pierre Auger Collaboration, Proc. 32nd ICRC (2011), arXiv:1107.4809v1.
20. The Pierre Auger Collaboration, Phys. Rev. Lett. **101** (2008) 061101.
21. I. Valiño, for the Pierre Auger Collaboration, Proc. 31^{st} ICRC, Łódź, Poland (2009),
22. G. Rodriguez, for the Pierre Auger Collaboration, UHECR Symposium CERN (2012) (to be published).
23. F. Salamida, for the Pierre Auger Collaboration, Proc. 32nd ICRC (2011), arXiv:1107.4809v1.
24. V. Verzi, for the Pierre Auger Collaboration, Proc. 33rd ICRC, Rio de Janeiro, Brazil, (2013); arXiv:1307.5059.
25. I. Maris, for the Pierre Auger Collaboration, UHECR Symposium CERN (2012) (to be published).
26. B. Kegl, for the Pierre Auger Collaboration, Proc. 33rd ICRC, Rio de Janeiro, Brazil, (2013); arXiv:1307.5059.
27. S. Ostapchenko, Nucl. Phys. B Proc. Suppl. **151**

(2006) 143.
28. M. Tueros, for the Pierre Auger Collaboration, Proc. 33rd ICRC, Rio de Janeiro, Brazil, (2013); arXiv:1307.5059.
29. V. de Souza, for the Pierre Auger Collaboration, Proc. 33rd ICRC, Rio de Janeiro, Brazil, (2013); arXiv:1307.5059.
30. E.J. Ahn, for the Pierre Auger Collaboration, Proc. 33rd ICRC, Rio de Janeiro, Brazil, (2013); arXiv:1307.5059.
31. K.-H. Kampert et al., Astropart. Phys. **42** (2013) 41.
32. R. Aloisio et al., JCAP10 (2012) 007.